High cycle fatigue and ratcheting interaction of laser powder bed fusion stainless steel 316L: Fracture behaviour and stress-based modelling

Zhang, M., Sun, C-N., Zhang, X., Wei, J., Hardacre, D. & Li, H.

Original citation & hyperlink:
Zhang, M, Sun, C-N, Zhang, X, Wei, J, Hardacre, D & Li, H 2019, 'High cycle fatigue and ratcheting interaction of laser powder bed fusion stainless steel 316L: Fracture behaviour and stress-based modelling' International Journal of Fatigue, vol. 121, pp. 252-264.
https://dx.doi.org/10.1016/j.ijfatigue.2018.12.016

DOI 10.1016/j.ijfatigue.2018.12.016
ISSN 0142-1123

Publisher: Elsevier

High cycle fatigue and ratcheting interaction of laser powder bed fusion stainless steel 316L: Fracture behaviour and stress-based modelling

Meng Zhang[1,2], Chen-Nan Sun[3], Xiang Zhang[4], Jun Wei[3], David Hardacre[2], Hua Li[1*]

[1] *Singapore Centre for 3D Printing, School of Mechanical and Aerospace Engineering, Nanyang Technological University, 50 Nanyang Avenue, Singapore 639798*
[2] *Lloyd's Register Singapore Pte Ltd, 1 Fusionopolis Place, #09-11 Galaxis, Singapore 138522*
[3] *Singapore Institute of Manufacturing Technology, A*STAR, 73 Nanyang Drive, Singapore 637662*
[4] *Faculty of Engineering, Environment & Computing, Coventry University, Coventry CV1 5FB, UK*

**Corresponding author: lihua@ntu.edu.sg*

Abstract

Variations in the physical and mechanical properties of parts made by laser power bed fusion (L-PBF) could be affected by the choice of processing or post-processing strategies. This work examined the influence of build orientation and post-processing treatments (annealing or hot isostatic pressing) on the fatigue and fracture behaviours of L-PBF stainless steel 316L in the high cycle fatigue region, i.e. 10^4 – 10^6 cycles. Experimental results show that both factors introduce significant changes in the plastic deformation properties, which affect fatigue strength via the mechanism of fatigue-ratcheting interaction. Cyclic plasticity is characterised by hardening, which promotes mean stress insensitivity and improved fatigue resistance. Fatigue activities, involving the initiation of crack at defects and microstructural heterogeneities, are of greater relevance to the longer life region where the global deformation mode is elastic. As the simultaneous actions of ratcheting and fatigue generate complex nonlinear interactions between the alternating stress amplitude and mean stress, the fatigue properties could not be effectively predicted using traditional stress-based models. A modification to the Goodman relation was proposed to account for the added effects of cyclic plasticity and was demonstrated to produce good agreement with experimental results for both cyclic hardening and softening materials.

Keywords: high cycle fatigue; ratcheting; stress-based model; stainless steel 316L; additive manufacturing

1. Introduction

Laser powder bed fusion (L-PBF) is an additive manufacturing (AM) technology for fabricating metal parts. High power laser raster scans rapidly to irradiate and consolidate loosely deposited metal powder layer by layer.

Dissipation of heat from the high temperature melt pool to the surrounding powder bed at 10^3 – 10^8 K/s [1] promotes the formation of non-equilibrium microstructure and unique mechanical properties. Process-induced ultrafine grains and dislocation network are key to the development of high tensile strength for L-PBF materials relative to the conventional counterparts [2, 3]. For low stacking fault energy materials such as stainless steel 316L, the stable dislocation network allows high strength to be achieved without compromising ductility [4]. However, large variations in mechanical performance across L-PBF-processed parts are possible due to the generation of interior and surface defects, microstructural heterogeneities and thermal stresses. Differences in processing conditions, such as laser settings [5], layer thickness [6], build orientation [7] and part geometry [8], are among the factors that could impinge on the part quality. As a result, despite the superior mechanical properties, significant variability in quality could lead to uncertainties in performance and heighten the risk of adopting the technology for structural applications.

The design and implementation of structural components cannot be done without considering the fatigue properties. The total strain-fatigue life equation indicates that the fatigue strength and ductility parameters govern the high cycle and low cycle fatigue properties respectively, and could be approximated by the corresponding static tensile values [9, 10]. While the parameter-based model provides a convenient means for fatigue assessment, correlations between the static tensile and fatigue parameters could not be easily obtained in practice as different L-PBF process variables could induce different microstructures and distinct cyclic deformation behaviours [11]. For instance, both heat treatment and unfavourable build orientation for L-PBF stainless steel 316L could lead to strength reduction, with the former being associated with the breaking down of the pre-existing microstructure [12, 13], and the latter with grain orientations that promote twinning [14]. The different metallurgical root causes could produce dissimilar effects on the fatigue responses, such that the resulting fatigue properties may not correlate directly with the static tensile properties.

Studies by Zhang et al. [15] had shown that the lower tensile strength after solution annealing subjects L-PBF stainless steel 316L to ratcheting, where the activation and accumulation of plastic strain takes place under stress-controlled cyclic loading with superimposed tensile mean stress. Cyclic hardening or softening affects the generation of plastic strain, which exhausts the ductility of the material with the progression of cycles till failure. As the high ductility of stainless steel 316L allows it to survive high cycle fatigue tests in spite of the plastic damage [16], ratcheting activities constitute essential aspects of the high cycle fatigue properties. As stress reduces and failure becomes increasingly dominated by the initiation and propagation of fatigue cracks [17, 18],

the interplay of fatigue and ratcheting impacts the overall fatigue life and should be considered for fatigue design and modelling. The mechanism of fatigue-ratcheting interaction could potentially be adopted as the mechanistic basis for a model that correlates L-PBF process- or post-processing-induced variations in tensile properties with the fatigue properties.

This work aims to expand the results from the previous study [15] by exploring further the roles of fatigue-ratcheting interaction on the high cycle fatigue properties of L-PBF stainless steel 316L. Besides solution annealing, hot isostatic pressing and build orientation were employed for evaluating the fracture behaviour and generalising the process/post-processing to fatigue relations. Based on the experimental results, the significance of fatigue-ratcheting interaction on the fatigue response was established. By analysing the relations among static tensile properties, cyclic stresses and the S-N properties, a stress-based model was proposed for fatigue prediction.

2. Materials and experimental methods

Gas-atomised stainless steel 316L powder with a predominantly spherical shape was purchased from Höganäs AB. Sample fabrication was performed on an EOS M290 L-PBF system installed with a Yb-fibre laser. The standard processing parameters, as recommended by the system manufacturer, were used for fabrication at a layer thickness of 20 μm on a preheated platform. As shown in Figure 1, rectangular blocks were prepared, with dimensions that provided sufficient margins for machining of the fatigue test samples by electrical discharge machining (EDM) wire cutting. The blocks were oriented at a small angle from the recoating direction to minimise uneven powder deposition due to interaction between the part and the recoater blade [19].

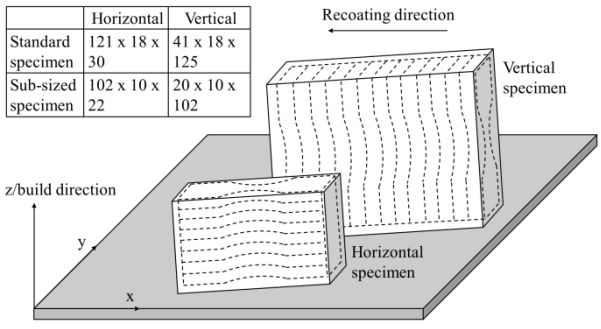

Figure 1 Orientation of rectangular blocks and fatigue test samples on the build platform; block dimensions (x × y × z) in mm for preparing standard and sub-sized samples are indicated.

After removal from the build platform, the blocks were machined by wire cutting into fatigue test sample geometries and manually grinded to remove residual surface oxides. With the exception of samples subjected to HIP, flat fatigue test specimens with tangentially blended fillets between the uniform gauge sections and the ends were designed in accordance to ASTM E466, with thickness 3 mm, gauge length 14 mm, width 7 mm, and overall length 119 mm. Due to the availability of test parts, sub-sized HIP samples were prepared, with thickness 3 mm, gauge length 12 mm, width 5 mm, and overall length 101 mm. Such difference in sample size had been reported to produce insignificant effects on the high cycle fatigue properties [20], though the use of sub-sized samples could lead to underestimated ductility values [21].

For examining the build orientation effects, both horizontal and vertical samples were prepared for the as-built and HIP conditions. As a maximum of eight samples were sliced from each block for the horizontal direction, causing the gauge sections to be located at different heights from the build platform, the influence of build height on part quality was examined. Porosity area fractions, based on image analysis of optical micrographs, and microhardness measurements were obtained at six different heights (of 5 mm intervals) on planes parallel to the build direction for samples in the as-built condition. Analysis of Variance (ANOVA) was performed and the results indicated no significant change of hardness and porosity conditions with build height at 95% confidence level. Thus, the samples were considered to be identical despite the different build heights.

The effects of annealing or hot isostatic pressing, collectively referred to as heat treatments in this work, were examined using horizontally-built samples only. Solution annealing were performed according to AMS 2750 at two different holding temperatures, i.e. 982 °C and 1093 °C, for 25 minutes in a vacuum furnace and subsequently gas quenched. HIP was done at 1190 °C and 145 MPa for four hours. Final grinding step was performed to remove surface contaminants generated from the thermal processes.

Load-controlled fatigue tests were carried out using sinusoidal loading at a frequency of 5 Hz on an MTS 810 hydraulic testing machine under ambient condition. Three different load ratios, R = -1, 0.1 and 0.7, were used for investigating the effects of mean stress. Samples that did not fail after 10^6 cycles were considered as run-outs. Static tensile tests were carried out in displacement-controlled mode with a crosshead speed of 0.2 mm/min using the same samples as the fatigue tests. Scanning electron microscope equipped with energy dispersive X-ray spectroscopy (SEM-EDX) was used for examining the fracture surfaces and chemical composition analysis.

3. Results and discussion

3.1 High cycle fatigue properties

3.1.1 Effect of build orientation

Static tensile properties of the samples are listed in Table 1. Noting the small standard deviations for samples with repeated tests, i.e. a maximum of ± 8 MPa for tensile strength and ± 3.4% for elongation to failure, single tests were conducted for conditions with limited samples, i.e. the vertical as-built and annealed samples. Orientation effects for the as-built condition are exemplified by the horizontal direction having higher strength but lower elongation to failure relative to the vertical direction, consistent with results from previous studies [14, 22]. The same tensile anisotropy applies to samples subjected to HIP, though the difference in ultimate tensile strength was reduced from 100 MPa for the as-built condition to 40 MPa after HIP, while the difference in ductility was reduced from 25% to 14%; yield strengths for the differently-oriented samples are nearly homogeneous after HIP. This indicates that HIP largely reduces but does not completely remove tensile anisotropy.

Table 1 Ultimate tensile strength, 0.2% offset yield strength and percentage elongation to failure of the samples. [Note: As-built vertical and annealed conditions consist of single test results.]

Sample	Ultimate tensile strength (MPa)	Yield strength (MPa)	Elongation to failure (%)
As-built (horizontal)	723 ± 7	586 ± 29	42.7 ± 2.2
As-built (vertical)	620	500	67.7
Annealed at 982 °C (horizontal)	673	440	51.9
Annealed at 1093 °C (horizontal)	665	420	56.1
Hot isostatically pressed (horizontal)	626 ± 3	283 ± 6	53.6 ± 1.4
Hot isostatically pressed (vertical)	582 ± 8	280 ± 8	67.2 ± 3.4

The distinct plastic deformation properties allude to orientation-dependent fatigue responses, especially under high stress conditions involving cyclic plasticity. To examine this effect, as-built samples were subjected to fatigue tests at R = -1, 0.1 and 0.7, where at the highest load ratio, the maximum applied cyclic stresses σ_{max} exceed the yield strength of the materials. For the HIP samples, tests were performed at R = 0.1 only, as the values of σ_{max} at this load ratio are above the materials' yield strength.

The S-N curves in Figure 2a show that for the as-built condition, orientation dependency is only discernible at R = 0.7, where the lower fatigue resistance of the vertical direction is indicative of its poorer capacity to withstand plastic deformation, in line with its lower static strength. This implies that tensile anisotropy translates to fatigue

anisotropy under plasticity-dominated failure. At R = 0.1 and -1, mean stress σ_m reduces while stress amplitude σ_a increases for the tested fatigue life region. As cyclic plasticity weakens with the lower mean stress, plasticity-induced fatigue anisotropy diminishes and the S-N data for the differently-oriented samples overlap. The higher amplitude stress instead resulted in greater contribution of fatigue activities on deformation [18] such that as stress reduces, the smaller plastic zone rendered the development of fatigue crack more sensitive to microstructural inhomogeneity at the crack tip [23]. This could be responsible for the variation in fatigue life at σ_a = 197 MPa and R = 0.1. It is to be noted that as single tests were conducted at different loads at R = 0.7, the validity of the trend shown for this loading condition should be confirmed by further experimental investigations.

For the HIP samples, no obvious fatigue anisotropy could be observed at R = 0.1 (Figure 2b), indicating that the tensile anisotropy was too small to inflict observable effects on the fatigue responses. However, at the smallest tested loading of σ_a = 162 MPa, the large variation in fatigue life, similar to the as-built samples, could again exemplify the transition from plasticity-dominated to fatigue-dominated deformation as cyclic stress reduces.

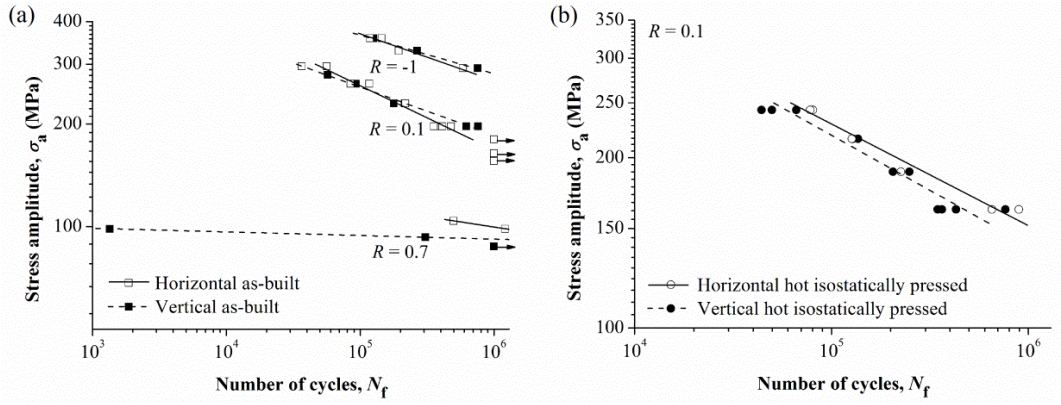

Figure 2 S-N curves of horizontal and vertical (a) as-built samples tested at different load ratios and (b) hot isostatically pressed samples tested at R = 0.1.

3.1.2 Effect of heat treatment

Heat treating led to strength reduction and ductility enhancement, as shown in Table 1. Comparing with the conventionally-manufactured forms, the ultimate tensile strength of heat treated L-PBF stainless steel 316L is still higher [24], indicating that only partial recrystallization and dislocation annihilation took place for the present heat treatment conditions [12, 25]. However, the yield strength for the HIP samples is nearly halved, which is a considerable reduction from the as-built or annealed conditions. Besides recrystallization and grain growth, coarsening of pre-existing nano-sized oxide inclusions could have contributed to this result [26] (detailed microstructural analysis is presented in Section 3.2.2).

The different tensile properties after heat treatment are clearly reflected in the finite life fatigue properties, as shown in Figure 3a (some of the data were adapted from the authors' prior work [16]). Fatigue resistance decreases with annealing temperature, where the reductions in fatigue life at σ_a = 200 MPa are about 42% and 47% for annealing at 982 °C and 1093 °C respectively. Test data of the HIP samples are generally within the range of the annealed samples despite the significantly lower yield strength. Replotting the S-N curves (Figure 3b) shows that the maximum applied cyclic stress to yield strength ratios increase to above unity after heat treatment. This is indicative of the significance of elastic-plastic deformation on the observed fatigue responses. Despite the reduced fatigue resistance, the HIP samples exhibit much better cyclic plastic performance than both the as-built and annealed conditions.

The fatigue limits after annealing did not deteriorate as much as the fatigue strength in the finite life region, as runouts were acquired at similar loadings for the annealed and as-built conditions. For these samples, the nominal elastic deformation mode was the driving failure mechanism. Fatigue limit for the HIP condition is lower, as the samples experienced plastic damage within the entire tested fatigue life region.

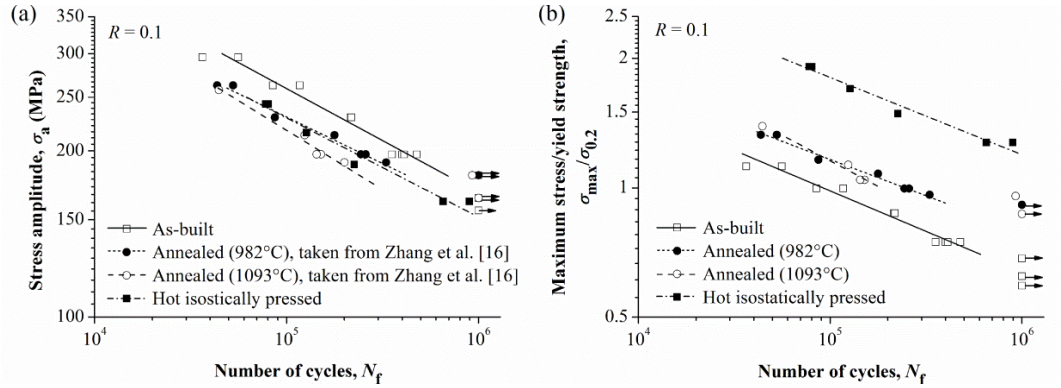

Figure 3 (a) S-N curves of as-built and heat treated horizontal samples tested at R = 0.1; (b) replotted S-N curves by normalising the maximum stress by the yield strength.

In summary, the effects of build orientation and heat treatment are strongly related to the interplay of ductile and fatigue fractures: differences in tensile properties induce changes in the S-N responses when the global plastic deformation mode is activated, such as for the as-built samples at R = 0.7 and the finite-life heat treated samples; fatigue activities become increasingly important as stress reduces and proceeds into the nominal elastic loading region, where the crack initiation mechanism is relevant. The fatigue fracture mechanisms relating to cyclic plasticity and crack-initiating defects are explored in greater details in the next section.

3.2 Fatigue failure mechanisms

3.2.1 Ratcheting behaviour

Cyclic plasticity was examined in terms of the mechanism of ratcheting, where the ratcheting strain ε_r was calculated using the expression:

$$\varepsilon_r = 0.5(\varepsilon_{min} + \varepsilon_{max}) \quad (1)$$

where ε_{min} and ε_{max} are the minimum and maximum axial strains of a particular cycle. It is to be noted that the strain values were calculated based on the machine's actuator output, and therefore are only valid for qualitative comparison and should not be taken as the actual values. Figure 4 shows the ratcheting strain against cycles to failure data of the samples. It can be seen that the ratcheting strain curves resemble that of creep deformation, consisting of the primary, secondary and tertiary deformation stages. The primary stage involves the development of a large initial strain followed by cyclic hardening, which serves to constrain further strain growth due to necking; the secondary stage is associated with a balance between cyclic hardening and softening, where stable or accelerated ratcheting rate could be achieved depending on the straining condition; significant cyclic softening occurs during the tertiary stage, triggering rapid failure of the sample.

For the as-built horizontal samples (Figure 4a), the secondary deformation phases at R = 0.1 are exemplified by close-to-zero ratcheting strains accumulation rates, as indicated by the nearly flat curves, while increasing the load ratio to R = 0.7 generated appreciable plastic deformation, giving rise to higher ratcheting strains and strain rates. Worth noting is the longer life at R = 0.7 than R = 0.1 despite the greater ratcheting damage. This is because though the larger mean stress exhausted the ductility of the material, the smaller stress amplitude, being the primary driver for the magnitude of the cyclic slip movement, was associated with less severe fatigue damage. Moreover, further strain reduction because of greater strain hardening at higher mean stress [27] alleviated the plastic damage due to ratcheting, resulting in the steady state ratcheting strain rates. As the mechanisms of ductility exhaustion, strain-induced hardening and fatigue competed against each other, the overall fatigue life improved at R = 0.7 despite the larger ratcheting strain. This result is indicative of the material's low sensitivity to the load ratio or mean stress comparing to the stress amplitude. Similar 'mean stress insensitivity' had been reported for conventionally produced stainless steel 316L [28, 29], suggesting that the general cyclic plastic response of the material is not affected by the L-PBF manufacturing route.

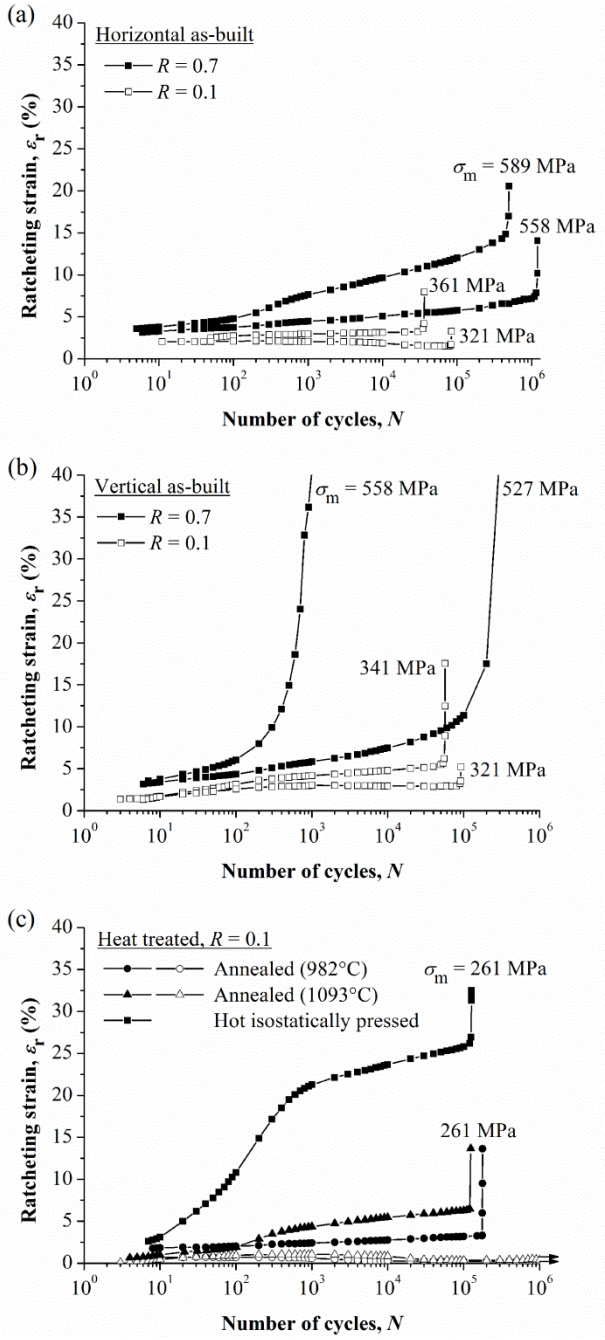

Figure 4 Ratcheting strains against load cycles of (a) horizontal and (b) vertical as-built samples, and (c) heat treated horizontal samples. [Filled symbols in (c) represent data for finite life samples tested at σ_m = 261 MPa while unfilled symbols represent data for runouts tested at σ_m = 221 MPa and 201 MPa for annealing at 982 °C and 1093 °C respectively.]

For the vertical samples, the lower yield strength incurred stronger ratcheting, as indicated by the higher ratcheting strains and strain rates relative to the horizontal direction (Figure 4b). At R = 0.7 and σ_m = 558 MPa, the ultimate tensile strength was exceeded, such that localised deformation and necking led to unconstrained increase in true stress and accelerated ratcheting caused failure to occur within 10^4 cycles. This explains the worse S-N properties of the vertical direction at R = 0.7, confirming that fatigue anisotropy was caused by the

different plastic properties of the materials. Again, in spite of the higher mean stress, the sample tested at R = 0.7 and σ_m = 527 MPa survived longer fatigue life than those tested at R = 0.1 because of the lower stress amplitude at R = 0.7, indicating that mean stress insensitivity is relevant regardless of the build orientation.

Figure 4c shows the ratcheting strains of the heat treated samples. For the runout samples, no ratcheting strain accumulation took place, confirming that the longer life properties and endurance limits are associated with the global elastic deformation mode. For the finite life samples, large initial strains, accompanied by longer primary deformation stages (exceeding 10^2 cycles) than the as-built conditions, were incurred. This is because unlike the as-built parts where the pre-existing dislocation network rearranged into a new configuration upon straining, gradual generation of dislocations took place in the absence of the dislocation network after heat treatment [4]. As the latter microstructure is associated with more sustained resistance to deformation and better cyclic hardening capacity [30], it allowed stable ratcheting strain rates to be achieved despite the large initial strains. Coupled with the enhanced ductility exhaustion capacity, this explains the better cyclic plastic performance after heat treatment, as shown in Figure 3b.

Worth noting is that notwithstanding the substantial strain induced in the HIP sample, its fatigue life is similar to the annealed samples. The higher applied stress relative to the yield strength could have incurred stronger cyclic hardening such that the rate of strain accumulation, as indicated by the slopes of the ratcheting strain curves in the secondary deformation stage, was not significantly increased as compared to the annealed conditions. This led to the similar finite life S-N properties of the HIP and annealed samples in Figure 3a, as well as the superior cyclic plastic performance of the HIP samples in Figure 3b.

3.2.2 Crack-initiating defects

Optical micrographs of the samples are shown in Figure 5. The as-built sample contained small sporadic gas pores on the order of 5 μm (Figure 5a). Such defects are typical of L-PBF-processed parts due to the entrapment of gas bubbles, e.g. the evaporation of low melting point elements or pre-existing nitrogen or argon gases in the powder feedstock [31]. No observable change in defect structure was observed for parts annealed at 982 °C (Figure 5b), but annealing at 1093 °C incurred significant increase in defect population, with a marginal increase in size to about 5 – 10 μm (Figure 5c). For the HIP sample (Figure 5d), submicron spherical voids with average size on the order of 0.5 μm constituted the prevailing defects.

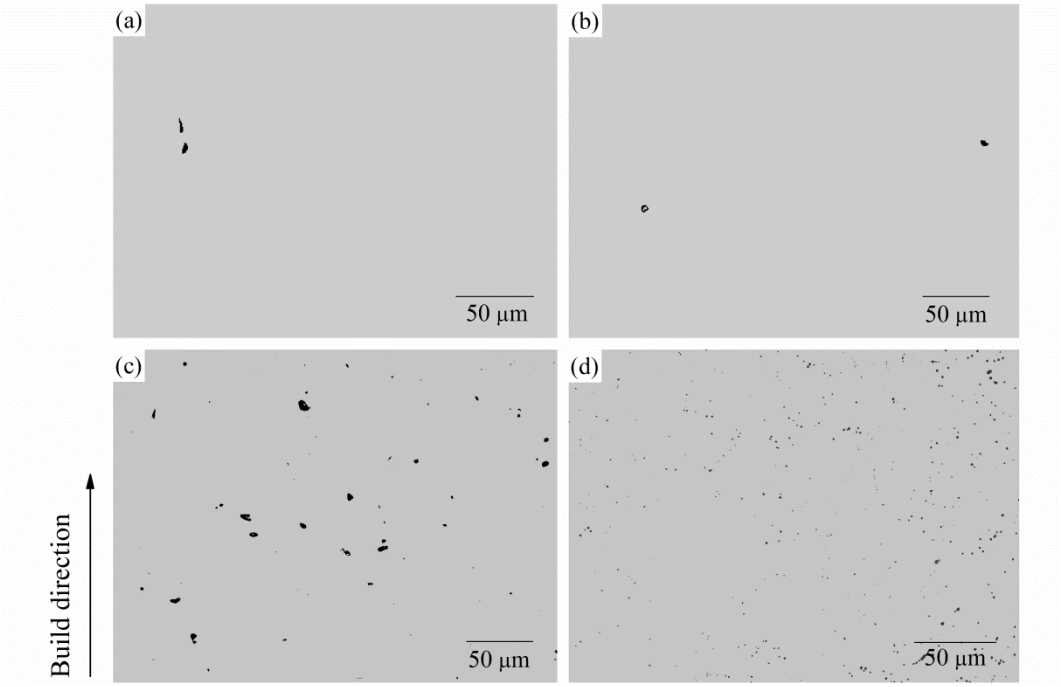

Figure 5 Optical micrographs of (a) as-built, (b) annealed (982 °C), (c) annealed (1093 °C) and (d) hot isostatically pressed samples. Dark pixels indicate defects.

The mechanism of defect formation for samples annealed at 1093 °C had been discussed in a prior work [15], where the increase in defect size was related to the nucleation and coalescence of pre-existing defects. As the L-PBF processing was conducted in an argon chamber, the low solubility of argon in iron prevented dissolution of argon gas into the material matrix [32], such that the gas pores expanded and coalesced into larger pores upon heating [33]. Besides gas pores and intercellular spaces, pre-existing or thermally-induced micro-cracks could also have acted as additional nucleation sites for gas diffusion and contributed to the increased defect density. Specifically, as stainless steel 316L contains strong oxide formers like Mn, Cr and Si, oxide layers formed on the powder surface during gas atomisation [34] could have prevented effective wetting of the melt pool and remained as discontinuities in the as-built parts. Thermal cracks could be generated via the reheat cracking mechanism [35, 36], where stress relaxation as temperature ramps up during annealing could cause intense plastic strain to be accumulated at weak sites, such as grain boundaries, and trigger intergranular cracking. This mechanism is especially relevant to L-PBF parts, considering the large amount of residual stress induced by the rapid cooling process [37, 38]. As the higher annealing temperature and the longer time taken to reach the temperature promoted the expansion and mobility of gas pores, as well as the formation of reheat cracks, such thermally-induced defects were observed in the higher-temperature-annealed parts only.

The high pressure HIP process led to closure of pre-existing defects but generated submicron spherical voids. As particles that occupied the submicron pits were dislodged during metallographic sample preparation, the rapid rupture region of a fatigue sample was examined, as shown in Figure 6. It can be seen that void nucleation occurred at submicron inclusions, e.g. site 'A' which, based on EDX analysis (Table 2), was concentrated in oxygen, silicon and manganese. Such silicon- and manganese-rich oxide particles had been observed in as-built stainless steel 316L [2, 39], where they existed on the nanoscale and were formed as a result of remnant oxide on the powder feedstock reacting with the alloying elements. HIP could have promoted the growth and coarsening of these nano-inclusions to submicron size [40, 41], which were critical in triggering micro-crack nucleation and led to the poor yield strength of the HIP samples.

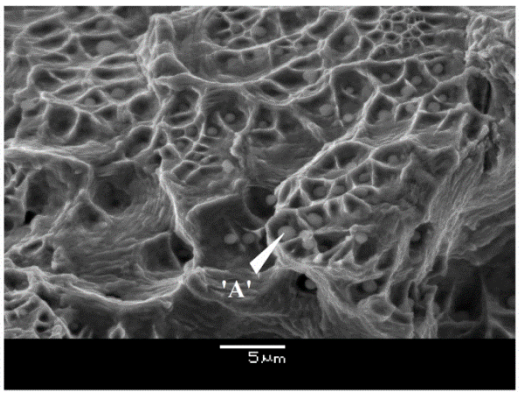

Figure 6 SEM fracture image of hot isostatically pressed fatigue sample showing void nucleation at spherical inclusions in the rapid fracture region.

Table 2 Elemental compositions (%wt) of regions 'A' and 'B' and the material matrix of hot isostatically pressed samples.

Region	O	Si	Cr	Mn	Fe	Ni	Mo
'A'	17.4	6.9	14.2	4.7	45.7	7.2	4.0
'B'	64.4	5.8	13.0	15.7	1.04	0.0	0.0
Matrix	0.0	1.87	18.3	1.1	63.3	10.8	4.6

The influence of the defects on fatigue crack initiation were examined by fractography analysis using samples tested at R = 0.1. For the as-built samples, the crack origins consist of features with dimensions on the order of 100 μm for both build orientations (Figure 7a-b). Enlarged views of the boxed regions reveal extensive cellular sub-grains (Figure 7c-d), indicating that intergranular fracture occurred at the macroscale grain boundaries. Such crack initiation mode was enabled by the presence of high dislocation density and segregated elements at the grain boundaries of L-PBF stainless steel 316L [3], which generated local stress concentration and promoted

cracking [11, 42]. In comparison, residual porosities in the as-built parts are much smaller relative to the macroscale grain boundaries and do not contribute to the formation of primary fatigue cracks.

The microstructure-driven crack initiation mode implies that microstructural heterogeneities were responsible for the variation in fatigue life under fatigue-dominated failure. Specifically, anisotropic microstructural arrangement, with respect to the crack propagation direction (from bottom to top of the images), operated at three length scales: at the macro-grain level, different macro-grain arrangements caused the size and shape of the crack origins to differ between the samples (Figure 7a-b); the sub-grain colonies, being sheet-like (as indicated in Figure 7c-d), affected the lengths of the local crack propagation paths, e.g. crack path for the vertical sample is longer because of propagation across the long edge of the sub-grain colony; individual cellular grains within the colonies are rod-like, which resulted in anisotropic crystallographic arrangements with respect to the loading direction and affected the local transgranular fracture mode, e.g. the vertical sample adopts a facetted surface because of stronger cleavage-type fracture. Such microstructural features influenced the crack initiation lives and generated scatter in the high cycle fatigue data.

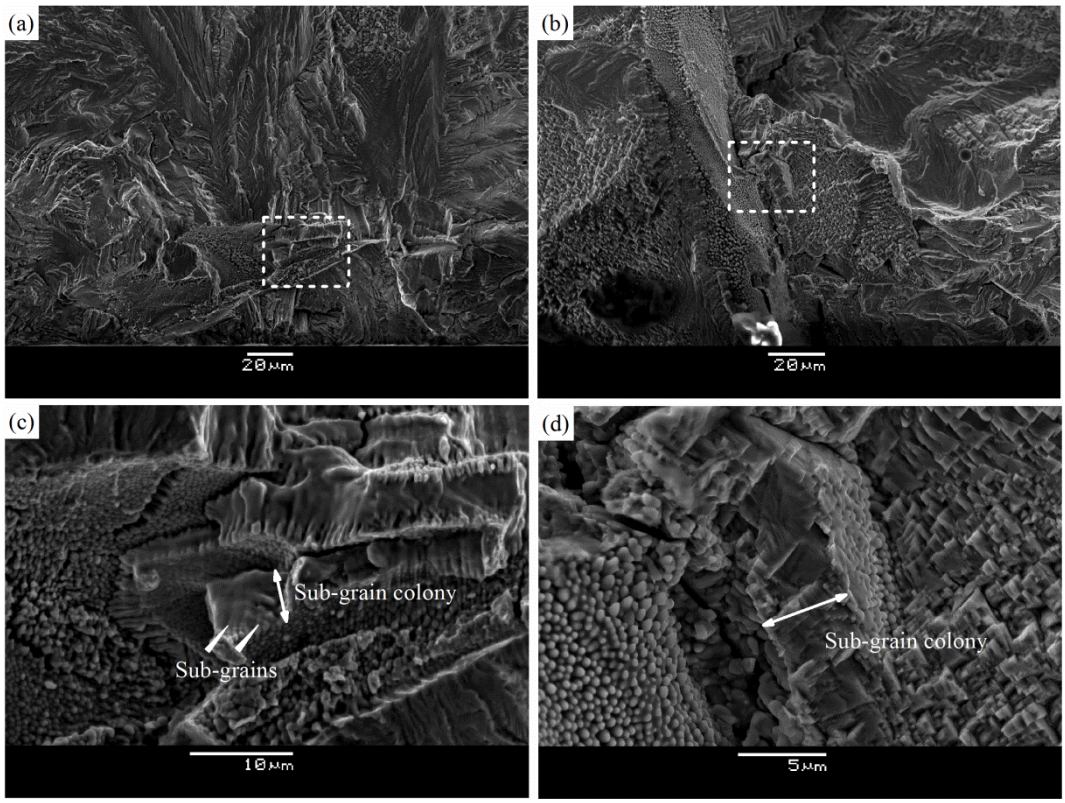

Figure 7 SEM fracture images of as-built (a) horizontal and (b) vertical samples; (c) and (d) are enlarged views of the boxed regions in (a) and (b) respectively. Tests were performed at σ_a = 197 MPa and R = 0.1. (a) and (c) had been published in a prior work [16].

Annealing at 982 °C preserved the intergranular crack initiation mode, as indicated in Figure 8a. The ultrafine cellular structures are no longer visible and the grain boundaries adopt a smoother profile, as heat treating had led to grain growth at the sub-grain level while the macro-scale grains remained intact [12, 25]. Since the annealing condition did not produce observable effects on the porosity structure, the macro-scale grain boundaries remained the weakest links under fatigue loading.

The higher annealing temperature of 1093 °C led to further consolidation of the sub-grains, as large grains on the order of tens of microns are traceable from the faint lines on the surface of the defect at the crack origin (Figure 8b). The compressed geometry and wrinkled surface eliminate the possibility of the defect being porosity or lack of fusion defect. Consider the substantial increase in defect at this annealing temperature, thermal defects, formed as a result of reheat cracking at the grain boundaries, could be responsible for the crack initiation. However, comparing with the defects in Figure 5c, the crack origin is considerably bigger. The mismatch in size could have resulted from stereological error because of measurements on two dimensional metallographic sections [43]. Also, as crack initiation seeks the maximum-occurring defects, large defects could have been missed because of the limited inspection area. In fact, smaller defects comparable in size with those in Figure 5c were found along the crack path [15]. The high annealing temperature could therefore have promoted the transition from intergranular- to defect-driven crack initiation, but as the fatigue limits of the as-built and annealed samples are similar based on runouts obtained at 10^6 cycles, the influence of the defects requires further investigation in the longer life region.

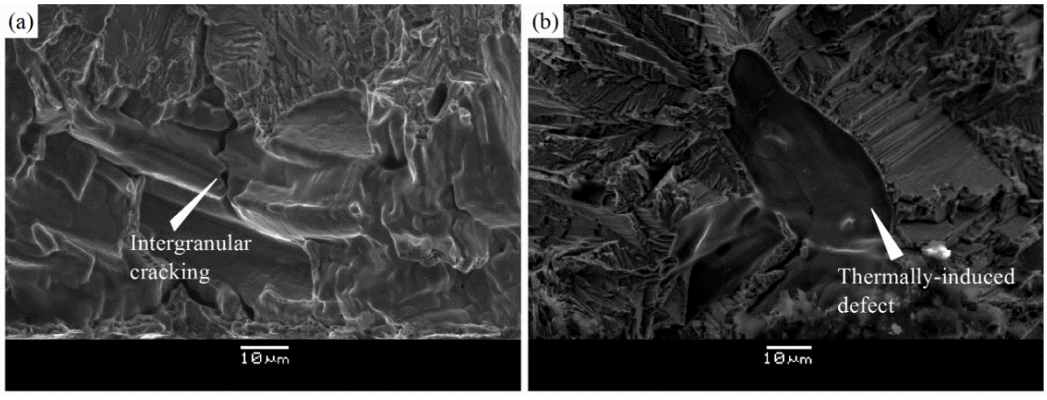

Figure 8 SEM fracture images of samples (a) annealed at 982 °C, showing intergranular crack initiation, and (b) annealed at 1093 °C, showing crack initiation from thermally-induced defect. Tests were performed at σ_a = 197 MPa and R = 0.1.

Fracture image of a horizontal HIP sample is shown in Figure 9a. Defect annihilation led to crack initiation via cyclic slip localisation. However, starting from the crack origin, the propagation path shows a rugged

morphology because of significant crack branching. Enlarged views of areas where the primary fatigue crack branched, as shown by the boxed regions, reveal closely-spaced spherical pits that were previously occupied by the coarsened oxide inclusions (Figure 9b-c). Besides lowering the yield strength, the inclusions, being highly clustered, also generated sufficient local stress concentration that promoted cracking under cyclic loading.

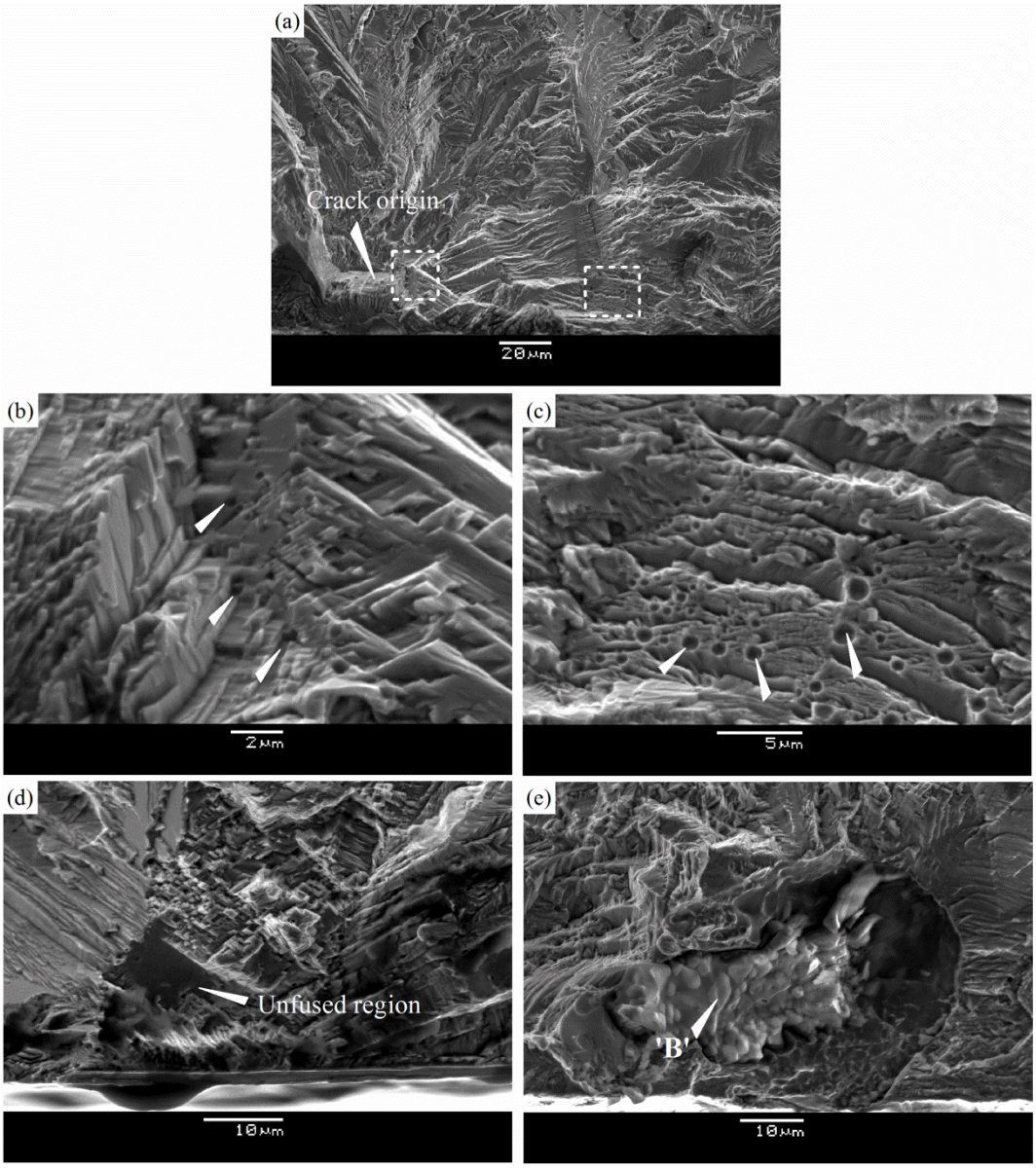

Figure 9 SEM fracture images of hot isostatically pressed samples. (a) Crack initiation and early crack propagation regions; (b)-(c) enlarged views of the boxed regions in (a) showing crack paths being directed by highly-clustered oxide inclusions; (d)-(e) crack initiations from unfused region and oxygen-contaminated particles respectively. Tests were performed at σ_a = 162 MPa and R = 0.1.

In addition, fractography analysis confirmed the fatigue life scatter at σ_a = 162 MPa to be caused by different crack origins. Figure 9d shows a vertical sample with fatigue life of 7.6×10^5 cycles failed from an unfused region on the order of 10 μm. The low-solubility argon gas could have prevented complete elimination of gas

pores by HIP, leaving behind defects with contacting interfaces [44]. In comparison, crack initiation from a large agglomeration of oxygen-rich particles (refer to EDX analysis of region 'B' in Table 2) led to significantly reduced fatigue life of 3.5×10^5 cycles (Figure 9e). Contaminated particles introduced into the powder feedstock during powder recycling could be one of the factors that led to the formation of such oxygen-rich compounds. Therefore, although HIP reduces the scale of critical defects from macro-scale grain boundaries or lack of fusion defects to submicron inclusions, parts become more sensitive to defects which could not be removed by HIP and are often less detectable, e.g. unfused regions or contaminants. This generated significant scatter in the S-N data under fatigue-dominated failure, rendering the fatigue properties less predictable.

3.3 Stress-based fatigue model

Results from the previous sections show that build orientation and post-processing treatments affect the high cycle fatigue properties of L-PBF stainless steel 316L primarily via the mechanism of fatigue-ratcheting interaction; critical defects and microstructure heterogeneities are generated but they are relevant to the longer life region where failure is dominated by fatigue activities. As the accumulative nature of ratcheting can lead to unexpected failure of engineering structures e.g. thinning and ovalisation of pipes [45], it becomes imperative to incorporate the plastic damage mechanism into fatigue modelling of L-PBF stainless steel 316L.

The effects of ratcheting could be modelled using the stress [46, 47], strain or energy [48-50] approaches. From the engineering standpoint, the stress-based approach is favoured as it allows the nominal stress associated with high cycle fatigue and ratcheting to be described explicitly. This section examines the applicability of traditional parameter-based stress models for predicting the S-N properties of L-PBF stainless steel 316L. Additional tests were done at R = -0.8, -0.5, -0.2 and 0.5 using horizontal as-built samples and a few heat treated samples to elucidate the stress-dependent effects of fatigue-ratcheting interaction. Based on the experimental results, a modified Goodman model was proposed for fatigue prediction in the 10^4 – 10^6 cycles life region.

3.3.1 Traditional models

The S-N relations of L-PBF stainless steel 316L were represented by straight lines on log-log plots. For fully reversed loading, i.e. R = -1, this power-law relation is described by the Basquin equation [51]:

$$\sigma_a = \sigma_f'(2N_f)^b \quad (2)$$

where σ_f' and b are the fatigue strength coefficient and the fatigue strength exponent respectively. The effects of mean stress σ_m can be estimated by adjusting the applied stress amplitude σ_a to the equivalent stress amplitude σ_a^{eq} according to the Goodman [52], Gerber [53] or Walker [54] equation, expressed respectively as:

Goodman equation: $\sigma_a^{eq} = \sigma_a/(1 - \frac{\sigma_m}{\sigma_b})$ (3)

Gerber equation: $\sigma_a^{eq} = \sigma_a/[1 - \left(\frac{\sigma_m}{\sigma_b}\right)^2]$ (4)

Walker equation: $\sigma_a^{eq} = \sigma_a \left(\frac{2}{1-R}\right)^{1-\gamma}$ (5)

where σ_b is the ultimate tensile strength and the Walker parameter γ is a material constant. Figure 10 shows the σ_a^{eq} against fatigue life plots obtained from applying these equations to the fatigue test data in this work and compared with the experimental Basquin curve for the horizontal as-built condition. [Note: γ = 0.527 was used as it fitted well the S-N data of small laboratory specimens [55]. As $\sigma_f' \approx \sigma_b$ for conventional steel [10, 56], σ_a^{eq} was normalised by the respective tensile strength values so that the fatigue data could be presented on the same plot; this is with the exception of the vertical as-built samples, for which the data were normalised by the tensile strength of the horizontal direction, as both directions have similar Basquin curves (Figure 2a).]

For the Goodman model (Figure 10a), reasonable predictions were obtained for the longer life samples at small load ratios only. As life decreases, the predicted σ_a^{eq} are always above the Basquin curve, similarly for the high load ratio cases, i.e. R = 0.5 and 0.7. This indicates that the samples performed better at these conditions than the Goodman relation, which is too conservative. In comparison, the Gerber model (Figure 10b) shifted the data points downwards such that it predicts the shorter life conditions effectively, but underestimated σ_a^{eq} as life increases. The Walker model (Figure 10c) produced the most accurate predictions, except for the heat treated samples at higher stresses and the vertical sample at R = 0.7.

The above results indicate that the Goodman and Walker models do not predict well for cases of significant ratcheting. This can be interpreted by noting that the Goodman model was formulated for high cycle fatigue where the global deformation is elastic. Since cyclic plasticity improves the fatigue properties of stainless steel 316L via the hardening mechanism, the conservative predictions of the Goodman model are reasonable. In addition, as the linear relation between the stress amplitude and mean stress for a specified number of cycles to failure, as assumed by the Goodman model, is not demanded by any physical mechanism [57], it becomes

inadequate when a wide range of stress covering both elastic and plastic deformation phenomena is involved [28, 47, 55, 58]. The same reasoning applies for the parabolic relation of the Gerber model, resulting in the models being effective for fatigue modelling of limited stress ranges only. The Walker model produced better predictions, probably because it was correlated with stress fields at crack tips [54], which represent more effectively the plastic deformation state. Nonetheless, the results suggests that it does not predict well when the extent of ratcheting strain accumulation is severe.

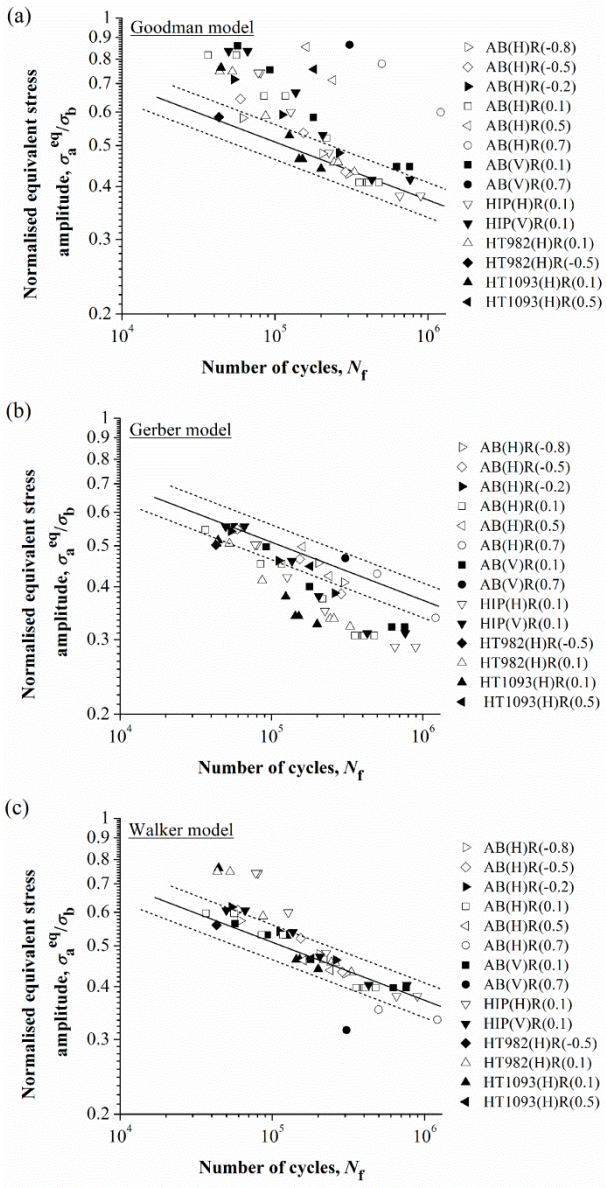

Figure 10 Normalised equivalent stress amplitude against fatigue life obtained from applying the (a) Goodman, (b) Gerber and (c) Walker models. Solid lines are the Basquin equations for the as-built condition and dotted lines indicate factor of two on life. [Meanings of symbol notations: AB – as-built; HT – heat treated; H – horizontal sample; V – vertical sample; R – load ratio, with values in brackets.]

3.3.2 Proposed model

As experimental results for L-PBF stainless steel 316L fall within the Goodman and Gerber predictions, and noting that these models differ in terms of the degree of the σ_m/σ_b term, i.e. 1 and 2 respectively, the nonlinearity arising from cyclic plasticity and the elastic-plastic interactions can be modelled by incorporating a stress-dependent function η to the degree of σ_m/σ_b, i.e.

$$\sigma_a^{eq} = \sigma_a/[1 - (\frac{\sigma_m}{\sigma_b})^{\eta}] \quad (6)$$

Ideally, η = 1 for pure elastic loading, i.e. the Goodman relation. The amount of deviation of η from unity serves to provide a quantitative measure of the nature and extent of cyclic plasticity. Specifically, as a material's fatigue performance under fatigue-ratcheting interaction is influenced by the combined effects of geometric softening, cyclic hardening/softening and fatigue activities, stronger cyclic hardening will give rise to larger η – in particular, η > 1 to reflect the conservative nature of the Goodman relation. In comparison, η for a cyclic softening material is lower as the greater accumulated strains are associated with more significant deformation and damage [59, 60], which render the Goodman relation less conservative. (See, for example, the Goodman predictions for cyclic hardening materials such as stainless steels 304 [47] and 316L [29], and cyclic softening materials such as Inconel 718 [47, 61] and a copper alloy [62]; for the cyclic softening materials, η could be smaller than 1 at low-to-moderate mean stresses.)

The relations between η and cyclic stresses for L-PBF stainless steel 316L are shown in Figure 11. For a fixed positive load ratio, η increases from 1 as mean stress (Figure 11a) or maximum stress (Figure 11b) increases because of the greater cyclic hardening at higher stresses. Data for the differently-oriented and heat treated samples nearly converged after normalising the stress terms by σ_b, as it allowed the extent of plasticity effect to be quantified. However, two observations could be made from Figure 11 that require further elaborations: (1) at positive load ratios, R dependency applies for the η vs. σ_m/σ_b plot, but not for the η vs. σ_{max}/σ_b plot; (2) at negative load ratios, as cyclic plasticity is not relevant because of the nominal elastic loading, the mechanism that invoked the changes in η needs to be investigated.

With regards to the first observation, it is to be reminded that besides cyclic hardening, mean stress insensitivity at higher load ratios is also attributable to the lower stress amplitudes, which incur less fatigue damage. Using σ_m as the correlation term accounts for the mean stress effects, i.e. geometric softening and cyclic hardening, but it does not resolve the reduced fatigue damage associated with the lower stress amplitudes. As a result, the

values of η at higher load ratios are lower when plotted against σ_m. Instead, the maximum stress, being the addition of the stress amplitude and mean stress, 'sums up' the effects of all operating mechanisms and led to better convergence of the data.

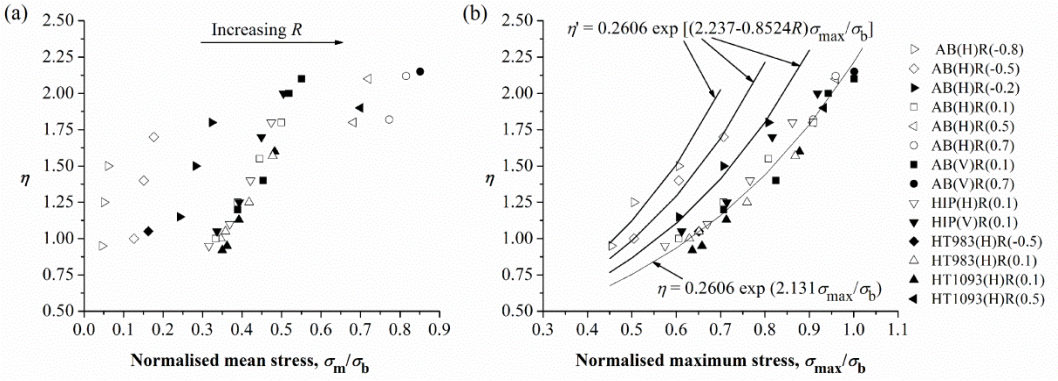

Figure 11 Variation of η with (a) σ_m and (b) σ_{max} at different load ratios. [Meanings of symbol notations: AB – as-built; HT – heat treated; H – horizontal sample; V – vertical sample; R – load ratio, with values in brackets; same legend applies to both figures.]

Based on this, σ_{max} could be employed for describing the effects of fatigue-ratcheting interaction on η using an exponential function, i.e.:

$$\eta = Kexp\left[c_0\left(\frac{\sigma_{max}}{\sigma_b}\right)\right] \quad (7)$$

where K and c_0 are material constants and their values are as shown in Figure 11b. Specifically, a positive c_0 is reflective of the direct relationship between η and σ_{max} due to hardening, while cyclic softening suppresses η at higher stresses and gives rise to less positive c_0; K dictates the order of magnitude of η, which, as mentioned, quantifies the deviation of actual material properties from the Goodman relation due to cyclic plasticity.

For the second observation, as failure at negative load ratios does not involve ratcheting, the symbol η' is used. Without further experimental validation, an attempt at explaining the observations is made here. A well-known mechanism that affects fatigue properties at small load ratios is crack closure. Roughness-induced crack closure could be enhanced for L-PBF parts because of the ultrafine-grained microstructure. As illustrated in Figure 12, for conventional coarse-grained materials, the propagation of short fatigue cracks is confined to the local microstructure, e.g. a single grain, such that the roughness-induced crack closure mechanism is not activated [63]. However, for L-PBF materials, the ultrafine sub-grains and differently-oriented sub-grain clusters have the effects of reducing the effective grain size, as well as generating asymmetric deformation at the crack tip (as demonstrated by the mixed intergranular and transgranular fracture modes). The formation of microscopically

rough fracture surfaces could have promoted roughness-induced crack closure in the crack wake [64, 65] and slowed down the crack growth rate [66]. The resulting improved fatigue resistance led to the apparent larger-than-unity η' values at the negative load ratios. This could further explain the R independency for the heat treated sample, e.g. refer to the data point at R = -0.5, where the coarsened grains after heat treatment created larger effective grain sizes and less pronounced closure. Moreover, since closure is not effective under large crack tip opening displacements [67-69], the R independency at positive load ratios in Figure 11b is consistent with this concept.

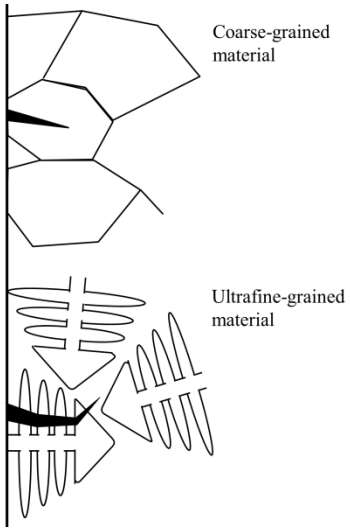

Figure 12 Schematic illustration of roughness-induced crack closure in coarse-grained material and ultrafine-grained laser powder bed fusion material with solidification microstructure.

While the fracture mechanisms leading to the R dependency at the negative load ratios require further investigation, the values of η' indicate that the effects on fatigue properties are nontrivial and should be taken into consideration. From Figure 11b, the relation could be modelled by incorporating R into Equation (7), i.e.:

$$\eta' = Kexp\left[(c_1 - c_2 R)\left(\frac{\sigma_{max}}{\sigma_b}\right)\right] \quad (8)$$

where c_1 and c_2 are empirical constants with values as shown in Figure 11b. It is to be emphasised that Equation (8) was derived purely from the empirical data and further study of the fracture mechanisms are necessary to support its validity.

Results from applying the proposed model to the fatigue test data in this work are shown in Figure 13a. Most of the predicted fatigue lives are within a factor of two of the experimental values, indicating significant improvements from the traditional models. The good prediction accuracy allows the constant fatigue life

diagrams to be plotted, as shown in Figure 13b. It can be seen that the σ_a vs. σ_m relation is life-dependent, unlike those assumed by the traditional models. At 10^4 cycles, the material is more fatigue resistant than that predicted by the Goodman equation because of cyclic plasticity at positive load ratios and the possible effects of roughness-induced crack closure at negative load ratios. At 10^6 cycles, difference between the predictions of the proposed model and the Goodman model diminishes, as failure is increasingly dominated by fatigue activities with elastic dominance and requires smaller adjustments for η. The slightly worse performance at the lower load ratios could be due to process-induced defects that promoted crack initiation, as discussed in Section 3.2.2, while the improved performance at the higher load ratios is again due to cyclic plasticity. In addition, as accounting for the load ratio effect, i.e. Equation (8), produced less conservative results, load ratio independency may be assumed for fatigue design.

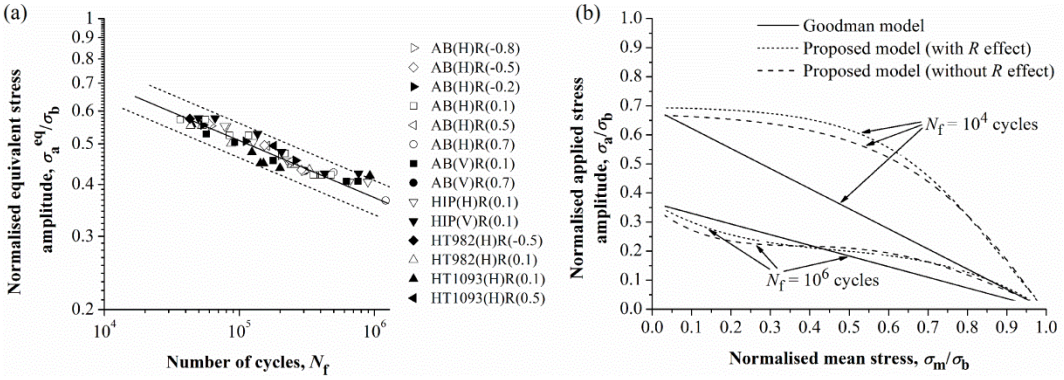

Figure 13 (a) Fatigue life predictions obtained using the proposed model (solid line is the Basquin line and dotted lines indicate factor of two on life); (b) comparison of the constant life diagrams for the Goodman and the proposed model. [Meanings of symbol notations in (a): AB – as-built; HT – heat treated; H – horizontal sample; V – vertical sample; R – load ratio, with values in brackets.]

3.3.3 Model validation

The proposed model was validated against (1) L-PBF stainless steel 316L test data reported by Spierings et al. [70], (2) rolled stainless steel 316L [20] and (3) other L-PBF alloys, including AlSi10Mg [71-73] and Inconel 718 [74, 75]. These materials were selected as the reported maximum cyclic stresses exceed the yield strengths in the high cycle fatigue region, making ratcheting the relevant failure mechanism. As listed in Table 3, all materials, except Inconel 718, displayed direct relationships between η and σ_{max}, as indicated by the positive c_0. The data fitted well to the form of exponential functions, as shown by the high coefficients of determination R^2. This is with the exception of Inconel 718, where the small R^2 is caused by the scatter of the limited experimental data. Note that the relative changes in c_0 are small, with $c_0 \approx 2.13$ for the positive c_0 materials.

Table 3 Material constants, coefficients of determination of the regression models and sources of data for validating the proposed model.

Materials	K	c_0	Range of η	R^2	Sources of data
L-PBF stainless steel 316L	0.2606	2.1309	0.9 – 2.2	0.967	Basquin equation: this work Positive R data: this work Validation data: Spierings et al. [70]
Rolled stainless steel 316L	0.4335	2.1301	2.2 – 3.1	0.898	All data adapted from Huang et al. [20]
L-PBF AlSi10Mg	0.1348	2.1325	0.2 – 0.6	0.934	Basquin equation: Uzan et al. [73] Positive R data: Aboulkhair et al. [72] Validation data: Maskery et al. [71]
L-PBF Inconel 718	1.4863	-0.2488	1.0 – 1.4	0.070	Basquin equation: Yadollahi et al. [75] Positive R data: Konečná et al. [74] Validation data: Konečná et al. [74]

The large positive c_0 for stainless steel 316L and AlSi10Mg suggests strong cyclic hardening, where conventionally manufactured stainless steel 316L cyclic hardens by strain-induced martensitic transformation [76, 77], while that for L-PBF AlSi10Mg pertains to precipitations-induced pinning effect [78]. The relatively constant c_0 values indicate that the use of σ_b for normalising the stress term provided effective scaling of the plasticity effects across the materials. The significance of adjusting for the stress-dependent effects of cyclic plasticity via c_0 and σ_b is demonstrated by the more comparable slopes of the predicted results with the gradients of the Basquin lines as compared to the Goodman results, as shown in Figure 14a-c. For Inconel 718, the close-to-zero c_0 is attributable to its cyclic softening properties [79], in line with the discussion that c_0 reduces with cyclic softening. In fact, this had led to the lower η such that the fatigue properties could be well predicted by the Goodman relation, as shown in Figure 14d.

The general improvements across the predictions of the proposed model over the Goodman model are due to calibrating η with the experimental data via the parameter K. Stainless steel 316L in the rolled form exhibits stronger hardening than the L-PBF form, as shown by the larger η, while the close-to-unity η for Inconel 718 is due to cyclic softening. However, the values of η for AlSi10Mg do not agree with its plastic properties, i.e. $\eta < 1$ even though it is cyclic hardening. This is because of the use of independent studies for deriving the parameters and validating the models, where differences in experimental conditions could affect the accuracy of both the Goodman and the proposed models. In particular, consider the L-PBF process's tendency for generating defects, different defect characteristics across the samples could be among the factors that lead to variations in the fatigue properties. In fact, this applies to the case of L-PBF stainless steel 316L, where possible defect-driven failure, as pointed out by Spierings et al. [70], could have given rise to the worse fatigue properties as compared

to the microstructure-driven failure pertaining to samples used in this work. The effects of such factors therefore need to be treated separately.

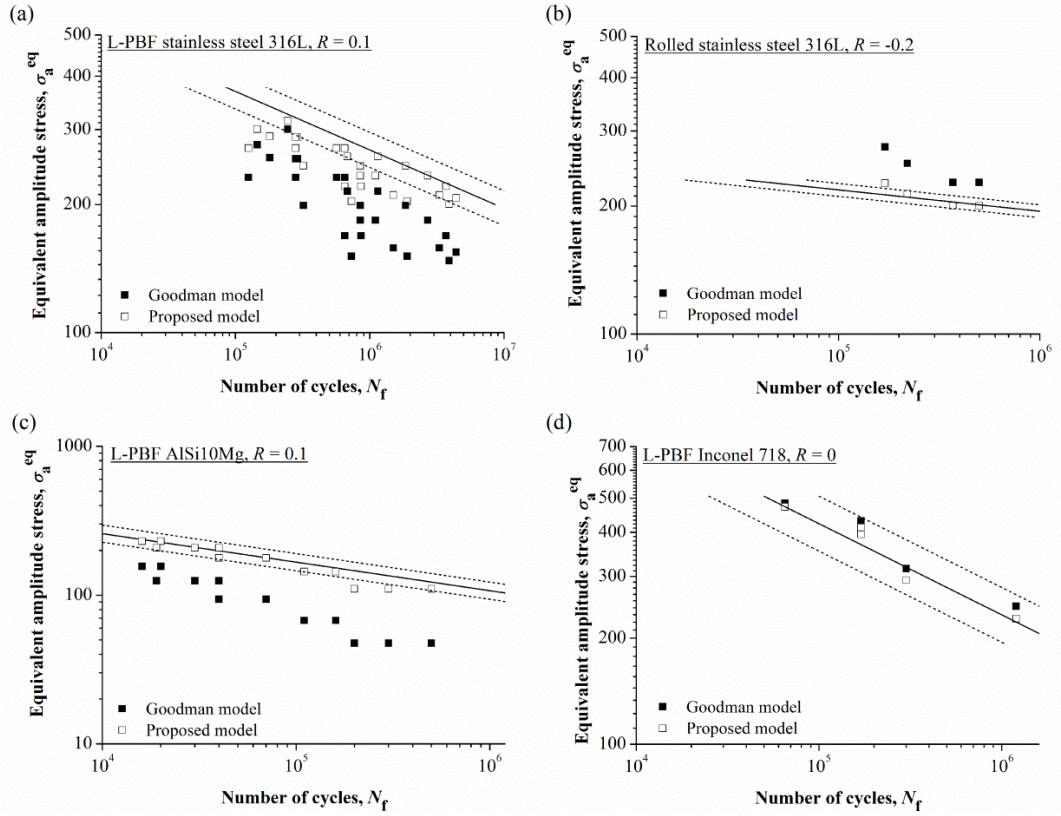

Figure 14 Validating the proposed model against (a) L-PBF stainless steel 316L, (b) rolled stainless steel 316L, (c) L-PBF AlSi10Mg and (d) L-PBF Inconel 718. Solid lines are the Basquin equations obtained from the references specified in Table 3 and dotted lines indicate factor of two on life.

4. Conclusions

This work examined the influence of build orientation and heat treatment (annealing or hot isostatic pressing) on the high cycle fatigue properties and fracture behaviours of L-PBF stainless steel 316L. The following conclusions can be made based on the results obtained:

1. For optimally processed parts devoid of critical crack-initiating defects, e.g. lack of fusion defects, the finite life S-N properties in the 10^4 – 10^6 life region is primarily affected by fatigue-ratcheting interactions, where ratcheting strain accumulation involving cyclic hardening is responsible for fatigue anisotropy and degraded fatigue resistance after heat treatment.
2. Defects and microstructural heterogeneities affect fatigue properties in the longer life region where the bulk deformation mode is elastic. After high temperature annealing, crack initiation occurs at thermally-induced

defects as the microstructural defects are removed by recrystallisation and grain regrowth. HIP causes previously benign defects to be exposed, resulting in larger scatter of the S-N data.

3. Traditional stress-based models such as the Goodman produced poor predictions when cyclic plasticity is significant. A modified Goodman equation was proposed by introducing an exponential function $\eta = f(\sigma_{max}/\sigma_b)$ to account for the material- and the stress-dependent effects of fatigue-ratcheting interaction.
4. While the model was developed based on fracture behaviours observed for changes in build orientation and heat treatment conditions, it is expected to describe the S-N properties of other L-PBF variables that incur the cyclic plastic deformation response. However, for factors contributing to the brittle defect-driven fatigue failure, the effects need to be treated separately.

Acknowledgement

This work was supported by the Singapore Economic Development Board (EDB) Industrial Postgraduate Programme (IPP).

References

[1] D. Gu, Y.-C. Hagedorn, W. Meiners, G. Meng, R.J.S. Batista, K. Wissenbach, R. Poprawe, Densification behavior, microstructure evolution, and wear performance of selective laser melting processed commercially pure titanium, Acta Mater. 60(9) (2012) 3849-3860.

[2] Y. Zhong, L. Liu, S. Wikman, D. Cui, Z. Shen, Intragranular cellular segregation network structure strengthening 316L stainless steel prepared by selective laser melting, J. Nucl. Mater. 470 (2016) 170-178.

[3] K. Saeidi, X. Gao, Y. Zhong, Z.J. Shen, Hardened austenite steel with columnar sub-grain structure formed by laser melting, Mater. Sci. Eng. A 625 (2015) 221-229.

[4] L. Liu, Q. Ding, Y. Zhong, J. Zou, J. Wu, Y.-L. Chiu, J. Li, Z. Zhang, Q. Yu, Z. Shen, Dislocation network in additive manufactured steel breaks strength–ductility trade-off, Mater. Today (2017).

[5] P. Hanzl, M. Zetek, T. Bakša, T. Kroupa, The influence of processing parameters on the mechanical properties of SLM parts, Procedia Engineering 100 (2015) 1405-1413.

[6] X. Shi, S. Ma, C. Liu, C. Chen, Q. Wu, X. Chen, J. Lu, Performance of high layer thickness in selective laser melting of Ti6Al4V, Materials 9(12) (2016) 975.

[7] A.H. Hassn, S. Christopher, H. Liang, Effect of build orientation on the surface quality, microstructure and mechanical properties of selective laser melting 316L stainless steel, Rapid Prototyping Journal 24(1) (2018) 9-17.

[8] A.E. Patterson, S.L. Messimer, P.A. Farrington, Overhanging features and the SLM/DMLS residual stresses problem: Review and future research need, Technologies 5(2) (2017) 15.

[9] J. Morrow, Cyclic plastic strain energy and fatigue of metals, Internal friction, damping, and cyclic plasticity, ASTM International1965.

[10] R. Landgraf, The resistance of metals to cyclic deformation, Achievement of High Fatigue Resistance in Metals and Alloys, ASTM International1970.

[11] M. Zhang, C.-N. Sun, X. Zhang, J. Wei, D. Hardacre, H. Li, Predictive models for fatigue property of laser powder bed fusion stainless steel 316L, Mater. Des. 145 (2018) 42-54.

[12] M. Montero Sistiaga, S. Nardone, C. Hautfenne, J. Van Humbeeck, Effect of heat treatment of 316L stainless steel produced by selective laser melting (SLM), Solid freeform fabrication symposium, Texas, USA, 2016.

[13] P. Krakhmalev, I. Yadroitsava, G. Fredriksson, I. Yadroitsev, Microstructural and thermal stability of selective laser melted 316l stainless steel single tracks, South African Journal of Industrial Engineering 28 (2017) 12-19.

[14] M. Shamsujjoha, S.R. Agnew, J.M. Fitz-Gerald, W.R. Moore, T.A. Newman, High strength and ductility of additively manufactured 316l stainless steel explained, Metall. Mater. Trans. A (2018) 1-17.

[15] M. Zhang, C.-N. Sun, X. Zhang, P.C. Goh, J. Wei, D. Hardacre, H. Li, Effect of heat treatment on fatigue crack initiation of laser powder bed fusion stainless steel 316L, MATEC Web of Conferences, EDP Sciences, 2018, p. 22006.

[16] M. Zhang, C.-N. Sun, X. Zhang, P.C. Goh, J. Wei, H. Li, D. Hardacre, Elucidating the relations between monotonic and fatigue properties of laser powder bed fusion stainless steel 316L, JOM 70(3) (2018) 390–395.

[17] Y. Liu, G. Kang, Q. Gao, Stress-based fatigue failure models for uniaxial ratchetting–fatigue interaction, Int. J. Fatigue 30(6) (2008) 1065-1073.

[18] P. Lukáš, L. Kunz, Effect of mean stress on cyclic stress-strain response and high cycle fatigue life, Int. J. Fatigue 11(1) (1989) 55-58.

[19] P.J. da Silva Bartolo, A.C.S. de Lemos, A.M.H. Pereira, A.J.D.S. Mateus, C. Ramos, C. Dos Santos, D. Oliveira, E. Pinto, F. Craveiro, H.M.C. da Rocha Terreiro, High value manufacturing: Advanced research in

virtual and rapid prototyping, Proceedings of the 6th International Conference on Advanced Research in Virtual and Rapid Prototyping, CRC Press, Portugal, 2013.

[20] J.-Y. Huang, J.-J. Yeh, S.-L. Jeng, C.-Y. Chen, R.-C. Kuo, High-cycle fatigue behavior of type 316L stainless steel, Materials transactions 47(2) (2006) 409-417.

[21] ASTM, E8/E8M Standard test methods for tension testing of metallic materials.

[22] I. Tolosa, F. Garciandía, F. Zubiri, F. Zapirain, A. Esnaola, Study of mechanical properties of AISI 316 stainless steel processed by "selective laser melting", following different manufacturing strategies, Int. J. Adv. Manuf. Technol. 51(5-8) (2010) 639-647.

[23] A. Pineau, S.D. Antolovich, Probabilistic approaches to fatigue with special emphasis on initiation from inclusions, Int. J. Fatigue 93 (2016) 422-434.

[24] ASM Handbook, Volume 1: Properties and Selection: Irons, Steels, and High-Performance Alloys, ASM International1990.

[25] K. Saeidi, X. Gao, F. Lofaj, L. Kvetková, Z.J. Shen, Transformation of austenite to duplex austenite-ferrite assembly in annealed stainless steel 316L consolidated by laser melting, J. Alloys Compd. 633 (2015) 463-469.

[26] X. Lou, P.L. Andresen, R.B. Rebak, Oxide inclusions in laser additive manufactured stainless steel and their effects on impact toughness and stress corrosion cracking behavior, J. Nucl. Mater. 499 (2018) 182-190.

[27] K.J. Miller, Cyclic behaviour of materials, Journal of Strain Analysis 5(3) (1970) 185-192.

[28] M. Kamaya, M. Kawakubo, Mean stress effect on fatigue strength of stainless steel, Int. J. Fatigue 74 (2015) 20-29.

[29] N. Miura, Y. Takahashi, High-cycle fatigue behavior of type 316 stainless steel at 288°C including mean stress effect, Int. J. Fatigue 28(11) (2006) 1618-1625.

[30] K. Hussain, E. De Los Rios, Monotonic and cyclic stress-strain behaviour of high strength steel, Metallurgical Science and Tecnology 11(1) (1993).

[31] B. Zhang, Y. Li, Q. Bai, Defect formation mechanisms in selective laser melting: A review, Chinese Journal of Mechanical Engineering 30(3) (2017) 515-527.

[32] S. Tammas-Williams, P. Withers, I. Todd, P. Prangnell, Porosity regrowth during heat treatment of hot isostatically pressed additively manufactured titanium components, Scripta Materialia 122 (2016) 72-76.

[33] H. Zhao, T. DebRoy, Pore formation during laser beam welding of die-cast magnesium alloy AM60B-mechanism and remedy, Welding Journal 80(8) (2001) 204-210.

[34] Y. Hedberg, M. Norell, J. Hedberg, P. Szakálos, P. Linhardt, I. Odnevall Wallinder, Surface characterisation of fine inert gas and water atomised stainless steel 316L powders: formation of thermodynamically unstable surface oxide phases, Powder Metall. 56(2) (2013) 158-163.

[35] A. Vinckier, A. Dhooge, Reheat cracking in welded structures during stress relief heat treatments, J. Heat. Treat. 1(1) (1979) 72-80.

[36] R. Skelton, I. Goodall, G. Webster, M. Spindler, Factors affecting reheat cracking in the HAZ of austenitic steel weldments, Int. J. Press. Vessels Pip. 80(7) (2003) 441-451.

[37] P.J. Withers, H.K.D.H. Bhadeshia, Residual stress. Part 2 – Nature and origins, Mater. Sci. Technol. 17(4) (2001) 366-375.

[38] Y. Liu, Y. Yang, D. Wang, A study on the residual stress during selective laser melting (SLM) of metallic powder, Int. J. Adv. Manuf. Technol. 87(1-4) (2016) 647-656.

[39] Z. Sun, X. Tan, S.B. Tor, W.Y. Yeong, Selective laser melting of stainless steel 316L with low porosity and high build rates, Mater. Des. 104 (2016) 197-204.

[40] K. Geenen, A. Röttger, W. Theisen, Corrosion behavior of 316L austenitic steel processed by selective laser melting, hot‐isostatic pressing, and casting, Materials and Corrosion 68(7) (2017) 764-775.

[41] A.J. Cooper, N.I. Cooper, A. Bell, J. Dhers, A.H. Sherry, A microstructural study on the observed differences in Charpy impact behavior between hot isostatically pressed and forged 304L and 316L austenitic stainless steel, Metall. Mater. Trans. A 46(11) (2015) 5126-5138.

[42] M. Zhang, C.-N. Sun, X. Zhang, P.C. Goh, J. Wei, D. Hardacre, H. Li, Fatigue and fracture behaviour of laser powder bed fusion stainless steel 316L: Influence of processing parameters, Mater. Sci. Eng. A 703 (2017) 251-261.

[43] Y. Murakami, S. Beretta, Small defects and inhomogeneities in fatigue strength: experiments, models and statistical implications, Extremes 2(2) (1999) 123-147.

[44] S. Shao, M.J. Mahtabi, N. Shamsaei, S.M. Thompson, Solubility of argon in laser additive manufactured α-titanium under hot isostatic pressing condition, Computational Materials Science 131 (2017) 209-219.

[45] G. Li, M. Berton, Cyclic behavior of a pipe section subjected to bending, ovalization or torsion loads in the case of a perfectly plastic material, Int. J. Press. Vessels Pip. 54(3) (1993) 363-386.

[46] S.K. Paul, S. Sivaprasad, S. Dhar, S. Tarafder, Ratcheting and low cycle fatigue behavior of SA333 steel and their life prediction, J. Nucl. Mater. 401(1-3) (2010) 17-24.

[47] M. Srimant Kumar, D. Krishna, K.K. Ray, Fatigue life estimation in presence of ratcheting phenomenon for AISI 304LN stainless steel tested under uniaxial cyclic loading, International Journal of Damage Mechanics 25(3) (2015) 431-444.

[48] X. Yuan, W. Yu, S. Fu, D. Yu, X. Chen, Effect of mean stress and ratcheting strain on the low cycle fatigue behavior of a wrought 316LN stainless steel, Mater. Sci. Eng. A 677 (2016) 193-202.

[49] Z. Xia, D. Kujawski, F. Ellyin, Effect of mean stress and ratcheting strain on fatigue life of steel, Int. J. Fatigue 18(5) (1996) 335-341.

[50] S. Zhu, Q. Lei, Q. Wang, Mean stress and ratcheting corrections in fatigue life prediction of metals, Fatigue Fract. Eng. Mater. Struct. 40(9) (2017) 1343-1354.

[51] O. Basquin, The exponential law of endurance tests, Proc Astm, 1910, pp. 625-630.

[52] J. Goodman, Mechanics applied to engineering, Longmans, Green1918.

[53] H. Gerber, Bestimmung der zulässigen spannungen in eisen-constructionen, Wolf1874.

[54] K. Walker, The effect of stress ratio during crack propagation and fatigue for 2024-T3 and 7075-T6 aluminum, Effects of environment and complex load history on fatigue life, ASTM International1970.

[55] N. Dowling, C. Calhoun, A. Arcari, Mean stress effects in stress‐life fatigue and the Walker equation, Fatigue Fract. Eng. Mater. Struct. 32(3) (2009) 163-179.

[56] R.W. Landgraf, Cyclic deformation and fatigue behavior of hardened steels, Department of Theoretical and Applied Mechanics (UIUC), 1968.

[57] T. Nicholas, J.R. Zuiker, On the use of the Goodman diagram for high cycle fatigue design, Int. J. Fract. 80(2) (1996) 219-235.

[58] I. Figge, An empirical equation relating fatigue limit and mean stress, NASA TN D-3883 (1967).

[59] T. Hassan, S. Kyriakides, Ratcheting of cyclically hardening and softening materials: I. Uniaxial behavior, Int. J. Plast. 10(2) (1994) 149-184.

[60] R. Kreethi, A.K. Mondal, K. Dutta, Ratcheting induced cyclic softening behaviour of 42CrMo4 steel, IOP Conference Series: Materials Science and Engineering 75(1) (2015) 012027.

[61] S.J. PARK, K.S. KIM, H.S. KIM, Ratcheting behaviour and mean stress considerations in uniaxial low-cycle fatigue of Inconel 718 at 649 °C, Fatigue Fract. Eng. Mater. Struct. 30(11) (2007) 1076-1083.

[62] C.B. Lim, K.S. Kim, J.B. Seong, Ratcheting and fatigue behavior of a copper alloy under uniaxial cyclic loading with mean stress, Int. J. Fatigue 31(3) (2009) 501-507.

[63] S. Suresh, R. Ritchie, A geometric model for fatigue crack closure induced by fracture surface roughness, Metall. Trans. A 13(9) (1982) 1627-1631.

[64] R. Pippan, A. Hohenwarter, Fatigue crack closure: a review of the physical phenomena, Fatigue Fract. Eng. Mater. Struct. 40(4) (2017) 471-495.

[65] Y. Weng, Ultra-fine grained steels, Springer Science & Business Media2009.

[66] G. Gray, J. Williams, A. Thompson, Roughness-induced crack closure: an explanation for microstructurally sensitive fatigue crack growth, Metall. Trans. A 14(2) (1983) 421-433.

[67] W. Elber, The significance of fatigue crack closure, Damage tolerance in aircraft structures, ASTM International, 1971, pp. 230-242.

[68] M. Katcher, M. Kaplan, Effects of R-factor and crack closure on fatigue crack growth for aluminum and titanium alloys, Fracture toughness and slow-stable cracking, ASTM International1974.

[69] T.T. Shih, R.P. Wei, A study of crack closure in fatigue, Eng. Fract. Mech. 6(1) (1974) 19-32.

[70] A. Spierings, T. Starr, K. Wegener, Fatigue performance of additive manufactured metallic parts, Rapid Prototyping Journal 19(2) (2013) 88-94.

[71] I. Maskery, N. Aboulkhair, C. Tuck, R. Wildman, I. Ashcroft, N. Everitt, R. Hague, Fatigue performance enhancement of selectively laser melted aluminium alloy by heat treatment, Solid Freeform Fabrication Symposium, Austin, Texas, USA, 2015, pp. 1017-1025.

[72] N.T. Aboulkhair, I. Maskery, C. Tuck, I. Ashcroft, N.M. Everitt, Improving the fatigue behaviour of a selectively laser melted aluminium alloy: Influence of heat treatment and surface quality, Mater. Des. 104 (2016) 174-182.

[73] N.E. Uzan, R. Shneck, O. Yeheskel, N. Frage, Fatigue of AlSi10Mg specimens fabricated by additive manufacturing selective laser melting (AM-SLM), Mater. Sci. Eng. A 704 (2017) 229-237.

[74] R. Konečná, G. Nicoletto, L. Kunz, A. Bača, Microstructure and directional fatigue behavior of Inconel 718 produced by selective laser melting, Procedia Structural Integrity 2 (2016) 2381-2388.

[75] A. Yadollahi, N. Shamsaei, Additive manufacturing of fatigue resistant materials: Challenges and opportunities, Int. J. Fatigue 98 (2017) 14-31.

[76] T. Michler, Formation of martensite in 304 grade stainless steels and their welds, Materialwissenschaft und Werkstofftechnik 38(1) (2007) 32-35.

[77] D. Hennessy, G. Steckel, C. Altstetter, Phase transformation of stainless steel during fatigue, Metall. Trans. A 7(3) (1976) 415-424.

[78] C. Cai, H. Geng, Z. Zhang, Temperature-dependent cyclic response and microstructure of AlSi10Mg(Cu) alloy, Mater. Charact. 141 (2018) 148-155.

[79] D. Gustafsson, J. Moverare, K. Simonsson, S. Sjöström, Modeling of the constitutive behavior of inconel 718 at intermediate temperatures, Journal of Engineering for Gas Turbines and Power 133 (2011).